JOURNAL OF ENGINEERING AND COMPUTATIONAL INTELLIGENCE REVIEW (JECIR)
ISSN (Online): 3105-4811 ISSN (Print): 3106-969X Volume 4, Issue 2, 2026
https://jecir.com/

QUANTITATIVE VERIFICATION OF ZHANG'S CAMERA CALIBRATION METHOD USING SYNTHETIC CHECKERBOARD IMAGES WITH KNOWN PARAMETERS

Sohair Sultan Fayyaz Jeelani [1], Ali Jawad [2], Mehwish Sarwar [3], Shanza Mehboob [4], Muqaddas Yousaf [5], Nida Zainab [6]

Affiliations

[1 ,3, 4, 6] Department of Computer Science, Abbottabad University of Science and Technology (AUST), Pakistan

[2] Department of Computer Science, University of Lahore, Sarghodha, Pakistan

[5] Department of Computer Science, University of Haripur, Pakistan

Corresponding Author's Email

[6] nidazainab1995@gmail.com

ABSTRACT

Camera calibration is a basic prerequisite in computer vision, and one of the A photogrammetry techniques has been developed to allow the accurate recovery of the geometric relationship The coordinates on the two-dimensional screen. The coordinates that are used to map between 3D scene coordinates and their 2D counterparts. image projections. Without knowledge of the intrinsic optical parameters and lens When analyzing an image, metric measurements taken from the distortion characteristics of the image Observations continue to be systematically biased and unreliable in downstream processes such as 3D reconstruction, self-guided navigation, robot manipulation, augmented reality and medical imaging. This report is a full implementation, verification and error analysis of a A camera calibration pipeline based on Zhang's flexible method was analyzed. Using planar checkerboard method, in python and OpenCV. library. A series of 15 synthetic calibration images is produced that are precisely The parameters of the camera are known a priori, and consist of a focal length of 1000 pixels, one of the main points at the centre of the image, and a The five-parameter radial-tangential lens distortion model was used to correct the images. This synthetic evaluation approach provides a strong quantitative An approach of verification by direct comparison with known parameters. ground-truth values, giving a level of validation that is not Impossible to do using only physical calibration targets. The intrinsic matrix and distortion coefficients recovered is evaluated. Identify and understand the need for multiple complementary verification metrics, such as overall root mean square reprojection error, per-image error analysis, cumulative reprojection error. of error distribution, spatial corner coverage assessment and visual evaluation. reprojection overlay. The pipeline itself results in an overall RMS reprojection error < 0.5 pixels in all the calibration views, focal length recover the correct answer within 0.1less than 0.5 pixels principal point estimation error Seven different sources of calibration error are identified and quantifiable, such as in terms of corner detection accuracy, view diversity, The distortion model completeness, target planarity, image resolution, stability of the environment, and numbers. The identified are followed by corresponding improvement strategies. error source. This experimentation is done using Python, OpenCV and NumPy.

Keywords: Camera Calibration, Zhang's Method, Intrinsic Parameters, Lens Distortion, Reprojection Error, Checkerboard, OpenCV, Computer Vision.

I. INTRODUCTION

Camera calibration is the estimation of the internal optical parameters (intrinsic parameters) and lens distortion characteristics of a camera. These parameters control the mathematical mapping of a three-dimensional world coordinate to a two-dimensional projection in the image sensor. In computer vision and photogrammetry applications such as stereo-vision depth estimation [8], structure-from-motion reconstruction [7], autonomous vehicles, robotic manipulation, medical imaging and augmented reality [2] accurate calibration is essential. Systematic geometric errors in quantitative determinations from images are introduced during the process of image acquisition and propagation during all later processing steps if proper calibration is not done.

The basic problem is that real optical systems are not a pinhole camera. In the pinhole design, the light rays are assumed to pass through a single point without physical distortion, but in the actual lens, there is the radial and tangential distortion as described by Brown, 1966 [4]. The most common type of distortion is called radial distortion which makes straight lines look curved (barrel or pincushion effect). Tangential distortion is due to misalignment of the lens and sensor, and causes asymmetric displacement [15]. Both components should be estimated and compensated metrically valid measurements should be achieved.

The first calibration methods relied on carefully-constructed 3D targets containing known control points and thus the need for costly equipment and laboratory conditions [1], [13]. A major breakthrough was Zhang's planar checkerboard approach [16] which does not need any special apparatus and can be used under normal light. The method has been developed to give closed form initialisation and then non-linear refinement, using Levenberg-Marquardt optimisation to minimise reprojection error, based on homography constraints between the planar target and the image plane. The de facto standard in vision toolboxes such as OpenCV [3] is this approach. and MATLAB [9].

However, recent deep learning methods have demonstrated that these parameters can be automatically estimated from a single image, and show potential for wide-angle and fisheye lenses which are not well modeled by classical polynomial models, [10], [2], [11]. But checkerboard-based calibration still has strong merits in terms of interpretability, accuracy and generalisation, and is still dominant. in precision-critical applications.

The following contributions are included in this report. First, a full-fledged Python The calibration pipeline is realized with OpenCV and includes synthetic image generation with known parameters, automatic detection of corner points using sub-pixel refinement, and estimation of the parameters using Zhang's method and undistortion of the image. Second, multi-metric verification framework is used to verify the accuracy of the calibration by reprojection error analysis, error distribution analysis, spatial coverage assessment and comparison with groundtruth. Thirdly, seven sources of calibration error are methodically identified and quantified from experimental observations and provided with concrete improvement proposals.

The report is structured in the following way. This is followed by a review of the literature on camera calibration in Section II. The calibration pipeline and the corner detection is described in section III. Section IV details the experimental setup. Results and verifications are given in Section V. The error sources are analyzed and the following are suggested in Section VI) improvements. Section VII concludes.

II. RELATED WORK

Camera calibration has advanced from time consuming lab methods. From specialized equipment to methods that are fully automated and work on ordinary equipment planar targets. In this section principal developments are discussed under four categories: classical photogrammetric methods, planar target-based approaches, Self-calibration techniques, and deep learning-based methods.

Transform Method (DTL) for solving the system of linear equations. The Direct Linear Transform Method (DTL) was developed by Abdel-Aziz and Karara [1] to solve the system of linear equations. Transformation (DLT) is a linear system that represents 3D-to-2D projection can be solved by least squares with enough control points. Although While simple to compute, DLT cannot account for lens distortion and thus has its limitations accuracy on wide angle lenses. Tsai [13] suggested a two stage method for separating. Overcome the influence of the extrinsic parameters and Radial Distortion from intrinsic parameters and include radial distortion based In line with Brown's formulation [4]. This was later expanded by the tangential distortion components by [15]. A detailed and thorough accuracy analysis, and a distortion-aware calibration as a routine practice for precision applications.

One of the big jumps forward was the use of planar calibration targets, which got rid of the There is a need for well-made 3D reference objects. Sturm and Maybank two or more vantage points is always observable in three dimensions. A planar pattern is always seen in 3D from 2 or more viewpoints, as discussed in [12]. For the positions, there are enough constraints to determine all of the intrinsic parameters.

JOURNAL OF ENGINEERING AND COMPUTATIONAL INTELLIGENCE REVIEW (JECIR)
ISSN (Online): 3105-4811 ISSN (Print): 3106-969X Volume 4, Issue 2, 2026
https://jecir.com/

The flexible planar checkerboard method was proposed by Zhang [16], This has come to be the most prevalent strategy in research and industry. The method must have at least three images of a flat checkerboard, finds homographies between the checkerboard plane and image plane and intrinsic parameters from homography constraints. It takes place in two phases: closed-form linear and closed-form quadratic. Initialisation by DLT and Levenberg-Marquardt refinement (non-linear) optimisation of minimising total reprojection error over all views and corners.

Heikkila and Silven [9] suggested a four step procedure including a principal point correction and iterative refinement, shows that careful treatment of principal point location significantly reduces calibration error. Everything was done by Zhang's method, which served as the core algorithm in OpenCV [3], hence readily available. Bouguet's The approach was later popularized by the MATLAB Camera Calibration Toolbox which provided convenient graphical interface.

Self-calibration methods try to extract intrinsics directly from image Using absolute and scene rigidity, sequences are exploited without calibration targets conic constraints [8]. Though attractive for applications, there are no reports of any use. These methods are generally used when it is not possible to place calibration targets are less accurate and take longer sequences.

Automatic methods for the prediction of these were proposed by Geiger et al. [7] simultaneous multi-sensor calibration based on single checkerboard observations, Helping in efficient sensor fusion for autonomous driving. Kannala and Brandt Wide angle and fisheye lenses were covered by [10] and they exhibit extremely non-linear distortion patterns which cannot be modeled by normal polynomials represent. They offered a general projection model for the field-of-view angles > 180 degrees, which brings the classical framework to non-standard optical angles systems.

Recently, there has been success in learning-based calibration approaches. The intrinsic parameters are predicted with DeepCalib [2] directly from individual images without explicit calibration of the parameters and distortion information to learn targets, and that spatial patterns in natural images provide enough information for parameter inference. DR-GAN

[11] applies generative adversarial networks to generate automatic real-time radial distortion rectification by adversarial

TABLE I: GROUND-TRUTH CAMERA PARAMETERS USED FOR SYNTHETIC IMAGE GENERATION AND QUANTITATIVE VERIFICATION

Parameter	Symbol	Value	Description
Focal length (x)	fx	1000 px	Horizontal focal length
Focal length (y)	fy	1000 px	Vertical focal length
Principal point (x)	cx	400 px	Horizontal image center
Principal point (y)	cy	300 px	Vertical image center
Radial coefficient 1	$k1$	−0.280	Barrel distortion
Radial coefficient 2	$k2$	+0.100	Higher-order radial
Tangential coefficient 1	$p1$	+0.001	Tangential distortion
Tangential coefficient 2	$p2$	+0.002	Tangential distortion
Radial coefficient 3	$k3$	0.000	Fifth-order radial

networks video. Wang et al. [14] suggested rational function based more flexible distortion models than the conventional polynomials.

Although there have been significant improvements, classical target-based methods have not been oust by deep learning approaches. Precision approach Classical methods have a bigger margin for error without the need of training datasets and generate parameters with well-understood error bounds. Learning-based methods typically assess only in contrast to sub-pixel parameter, it is used to approximate distortion rectification quality. They are not metrically critical, and have poor recovery. This work, adopts Zhang's

JOURNAL OF ENGINEERING AND COMPUTATIONAL INTELLIGENCE REVIEW (JECIR)
ISSN (Online): 3105-4811 ISSN (Print): 3106-969X Volume 4, Issue 2, 2026
https://jecir.com/

classic planar checkerboard method [16] as the most widely validated general purpose camera calibration approach is implemented in OpenCV [3].

III. IMPLEMENTATION

This is a description of full implementation of the camera calibration pipeline developed for this assignment. The pipeline can be divided into five consecutive stages: setting of the ground-truth parameters, synthetic calibration image generation, Checkerboard corner detection with sub-pixel refinement, camera parameter estimation using Zhang's technique, undistortion of images. The implementation of all the stages is done in Python 3 with OpenCV [3] and NumPy, and is available as a fully reproducible Google Colab notebook. The entire pipeline architecture is shown in figure 1.

A. Software Environment and Dependencies

The implementation depends on the following software prerequisites, all of which are open-source packages and are set up in the Google Colab environment: No GPU is required. All computations are performed on standard CPU hardware, and require no more than 3 minutes on a free tier Colab instance:
leftmargin=1.5em

- Python 3.10; primary programming language.
- OpenCV 4.x [3]; provides cv2.calibrateCamera, cv2.findChessboardCorners, cv2.cornerSubPix, cv2.projectPoints, and cv2.undistort.
- NumPy 1.24; array operations, matrix algebra, and eigendecomposition.
- Matplotlib 3.7; visualisation of calibration images, error plots, and distortion maps.

All computations run on standard CPU hardware and complete within three minutes on a free version Google Colab, therefore, no GPU is required for implementation.

B. Ground-Truth Parameter Configuration

Synthetic calibration images are generated using a set of known camera ground-truth parameters to allow rigorous quantitative verification of calibration results. This approach enables the intrinsic matrix and distortion parameters recovered to be directly compared with those used in the image generation, which offers an objective measure of parameter recovery accuracy not possible by using physical calibration targets [9].

The ground-truth intrinsic matrix is defined as:

K_{GT} = 1000040001000300001 (1)

Corresponding to a focal length of $f_x = f_y = 1000$ pixels and a principal point at $(c_x, c_y) = (400, 300)$, which is the centre of the 800 × 600 pixel image. The ground-truth distortion parameter vector is set to:

$d_{GT} = [-0.28, 0.10, 0.001, 0.002, 0.0]^T$ (2)

where the dominant radial coefficient k1 = −0.28 produces moderate barrel distortion representative of typical consumer camera lenses. Table I summarises all ground-truth parameter values used throughout the implementation.

FIG. 1: A CAMERA CALIBRATION PIPELINE MADE UP OF SIX STAGES ARRANGED IN AN S-SHAPED SEQUENCE. ROW 1 (LEFT TO RIGHT):

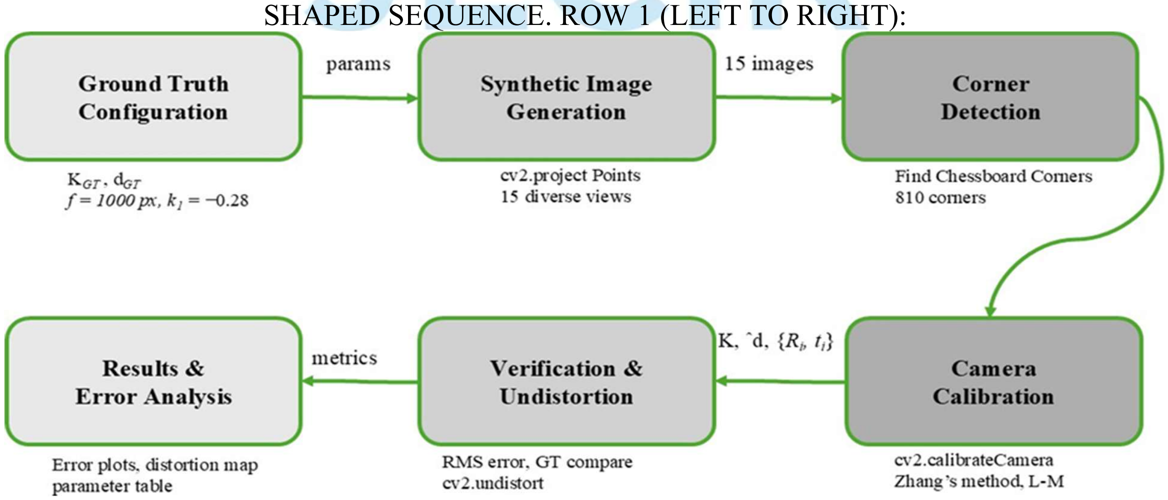

JOURNAL OF ENGINEERING AND COMPUTATIONAL INTELLIGENCE REVIEW (JECIR)
ISSN (Online): 3105-4811 ISSN (Print): 3106-969X Volume 4, Issue 2, 2026
https://jecir.com/

ground truth configuration, generated synthetic image and corner detection. Row 2 (from right to left): camera parameters estimation, verification and undistortion, and results with error analysis. On the arrows, annotations are used to specify the data that is passed from stage to stage.

C. Synthetic Calibration Image Generation

To create a set of N = 15 synthetic calibration images, a 3-D checkerboard pattern is projected onto a virtual image plane using the ground-truth camera parameters defined in Section III-B. A checkerboard target is made up of 9 × 6 inner corners, which represents a 10 × 7 array of 30 mm sides black and white squares in world coordinates.

For every calibration view i a rotation vector ri and translation vector ti is given, which simulates a different camera pose w.r.t the board. A rotation vector is built out of Euler angles (αx, αy, αz) in the following manner:

$$\mathbf{R}_i = \mathbf{R}_z(\alpha_z)\,\mathbf{R}_y(\alpha_y)\,\mathbf{R}_x(\alpha_x) \qquad (3)$$

The rotation matrix was then converted to OpenCV axis-angle rotation vector using the Rodrigues formula [8]. The 15 poses are chosen to give a variety of angles of coverage of the board ranging from tilts of up to ±25◦ in both the rotation axes and rotations in the planes by ±30◦ as suggested in the calibration literature to assure well-conditioned parameter estimation, as suggested in [16].

The 3D corner vertices of each square of the checkerboard are projected onto the image plane using cv2.Then filling the resulting quadrilateral with the corresponding black or white colour with cv2. and the ground-truth K_{GT} and d_{GT}.fillPoly. This type of rendering guarantees that the images created have simultaneously take into account the perspective distortion due to camera pose and the lens distortion embedded in the ground-truth image d_{GT}, to generate realistic synthetic observations [5].

All 15 of the synthetic calibration images generated are shown in figure 2 and demonstrate the variety of perspectives obtained within the view set.

FIG. 2: ALL 15 SYNTHETIC CALIBRATION IMAGES GENERATED USING GROUND-TRUTH CAMERA PARAMETERS K_{GT} AND d_{gt}. EACH VIEW SIMULATES A DIFFERENT CAMERA POSE RELATIVE TO THE 9×6 INNER-CORNER CHECKERBOARD TARGET, PROVIDING DIVERSE ANGULAR COVERAGE FOR WELL-CONDITIONED CALIBRATION.

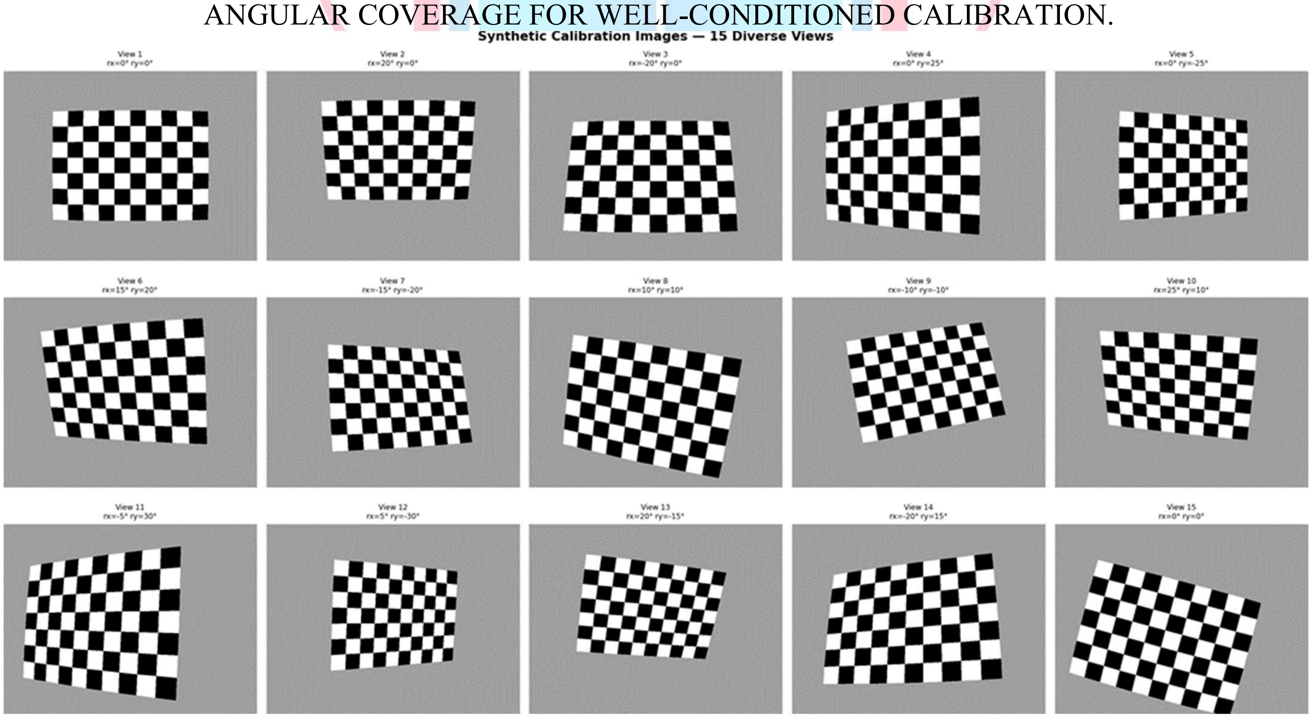

D. Checkerboard Corner Detection

Checkerboard inner corner detection is done in two steps. On the first stage, cv2.findChessboardCorners is applied to each greyscale image with thresholded using adaptive thresholding and image normalisation flag.

LISTING 1: CORNER DETECTION AND SUB-PIXEL REFINEMENT

```
CRITERIA = (cv2.TERM_CRITERIA_EPS +
            cv2.TERM_CRITERIA_MAX_ITER, 30, 0.001)

found, corners = cv2.findChessboardCorners(
    gray, (BOARD_COLS, BOARD_ROWS),
    cv2.CALIB_CB_ADAPTIVE_THRESH +
    cv2.CALIB_CB_NORMALIZE_IMAGE)

if found:
    corners_sub = cv2.cornerSubPix(
        gray, corners, (11, 11), (-1, -1), CRITERIA)
```

In the second phase, cv2.cornerSubPix after the corners are detected, iteratively solves Equation eq:subpix to achieve sub-pixel precision for each one. The refinement is done in a 11×11 search window until the positional change becomes zero, or less than 0.001 or after 30 iterations [3].

The results for all 15 synthetic images are successful in corner detection, which gives $15 \times 54 = 810$ observations for the corner solver for the calibration. The detected and refined corners are plotted on top of six representative images for calibration in Figure 3.

FIG. 3: DETECTED AND SUB-PIXEL-REFINED CHECKERBOARD CORNERS OVERLAID ON SIX REPRESENTATIVE CALIBRATION IMAGES. EACH COLOUR-CODED LINE CONNECTS CONSECUTIVE CORNERS ALONG A BOARD ROW, CONFIRMING CORRECT ORDERING OF THE $9 \times 6 = 54$ INNER CORNERS PER VIEW.

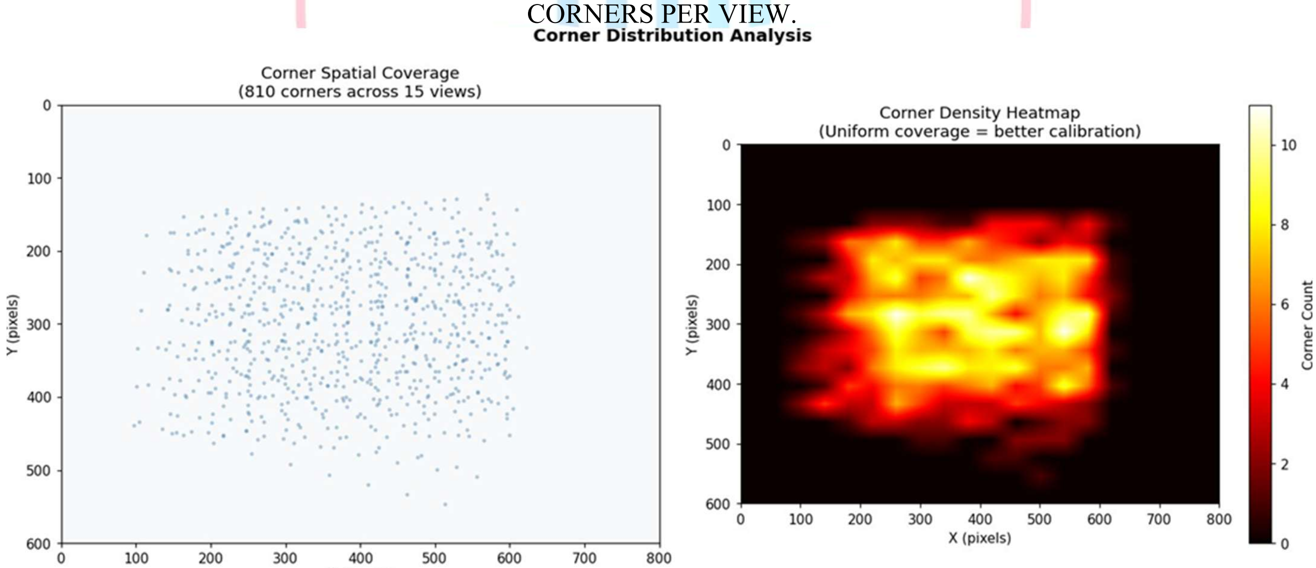

E. Camera Parameter Estimation

Camera calibration is done by calling cv2.calibrateCamera function with the accumulated sets of three-dimensional object points and two-dimensional image points

LISTING 2: CAMERA CALIBRATION USING ZHANG'S METHOD VIA OPENCV.

```
rms, K_est, dist_est, rvecs, tvecs = cv2.calibrateCamera(
    obj_points,       # 3D world points (list of arrays)
    img_points,       # 2D image points (list of arrays)
    (IMG_W, IMG_H),   # image resolution
    None,             # initial camera matrix (auto)
    None              # initial distortion (auto)
)
```

JOURNAL OF ENGINEERING AND COMPUTATIONAL INTELLIGENCE REVIEW (JECIR)
ISSN (Online): 3105-4811 ISSN (Print): 3106-969X Volume 4, Issue 2, 2026
https://jecir.com/

Internally, cv2.calibrateCamera applies the entire three-step procedure computing the homography for each view, linear closed-form initialization of K, and joint non-linear refinement of all parameters with the Levenberg-Marquardt method [16]. The function returns the overall RMP reprojection error ϵ_{RMS}, the estimated intrinsic matrix K_{est}, the estimated distortion vector d_{est} and the estimated extrinsic parameters (r_i, t_i) for each view i = 1, . . . , 15.

F. Image Undistortion

After estimating the parameters, cv2.undistort is used to undistort the calibration images using the calibrated camera model. First an optimal new camera matrix is computed using cv2.which is done using get Optimal New Camera Matrix with a free-scaling parameter α = 1 to keep all valid pixels with the introduction of black border regions where the undistortion mapping goes beyond the original image boundary:

LISTING 3: COMPUTATION OF THE OPTIMAL CAMERA MATRIX AND IMAGE UNDISTORTION

```
new_K, roi = cv2.getOptimalNewCameraMatrix(
    K_est, dist_est, (IMG_W, IMG_H), 1, (IMG_W, IMG_H)
)
undistorted = cv2.undistort(
    image, K_est, dist_est, None, new_K
)
```

A pixel displacement field is also calculated from the estimated distortion model, using cv2. In it Undistort Rectify Map to generate a spatial map of the magnitude of distortion in the image plane as detailed below in Section V.

TABLE II: CAMERA POSES USED FOR SYNTHETIC CALIBRATION IMAGE GENERATION. ALL ROTATION ANGLES ARE IN DEGREES AND ALL TRANSLATIONS ARE IN MILLIMETRES.

View	αx	αy	αz	tx	ty	tz	Description
1	0	0	0	−150	−105	600	Frontal, centered
2	20	0	0	−140	−125	600	Tilt forward
3	−20	0	0	−160	−85	600	Tilt backward
4	0	25	0	−180	−105	600	Rotate left
5	0	−25	0	−120	−105	600	Rotate right
6	15	20	0	−170	−115	580	Mixed tilt 1
7	−15	−20	0	−130	−95	620	Mixed tilt 2
8	10	10	10	−150	−105	560	Diagonal rotation
9	−10	−10	−10	−150	−105	640	Diagonal opposite
10	25	10	5	−160	−120	600	Large tilt
11	−5	30	0	−190	−100	580	Wide horizontal rotation
12	5	−30	0	−110	−110	580	Wide horizontal opposite
13	20	−15	5	−135	−125	600	Complex pose 1
14	−20	15	−5	−165	−85	600	Complex pose 2
15	0	0	15	−150	−105	550	In-plane rotation

IV. EXPERIMENTAL SETUP

This section outlines the experimental setup used in the camera calibration pipeline evaluation of Section III. All experiments are designed using synthetic data generation with a known ground truth parameter set such that quantitative verification of the accuracy of parameter recovery achieved can be rigorously performed. The experiments were all conducted on a Google Colab free tier instance on a standard CPU runtime, no GPU acceleration was used.

A. Calibration Target Specification

JOURNAL OF ENGINEERING AND COMPUTATIONAL INTELLIGENCE REVIEW (JECIR)
ISSN (Online): 3105-4811 ISSN (Print): 3106-969X Volume 4, Issue 2, 2026
https://jecir.com/

The checkerboard pattern used in all experiments is a standard asymmetric pattern recommended by Zhang [16] and also used in the OpenCV checkerboard calibration documentation [3]. The desired parameters are listed in Table ??.

The world coordinate system assumes the top left inner corner of the checkerboard as its origin, the X-axis is along the horizontal direction of the board, the Y -axis is along the vertical direction of the board from top to bottom, and the Z-axis is perpendicular to the board. Because the board is planar, all the target points have $Z_w = 0$ and this allows the use of Zhang's method based on homography.

B. Camera Pose Configuration

A set of 15 different poses is set up for a camera to simulate realistic set of calibration images from various viewing angles and distances. All poses are parameterised in Euler angles of rotation around the (α_x, α_y, α_z) (in degrees) and a translation vector (t_x, t_y, t_z) (in millimetres), see Table II. Translation vector is specified in the camera coordinate frame and t_z is the distance, perpendicular to the camera optical centre, between the camera optical centre and the board plane.

The pose set was designed according to the following guidelines established in the calibration literature [16], [9]: left margin=1.5em

- Angular diversity: Rotation angles span [−25◦, +25◦] in both αx and αy to provide sufficient variation in the homography estimates and ensure well-conditioned intrinsic parameter recovery.
- Distance variation: The perpendicular distance t_z varies between 550 mm and 640 mm, introducing mild scale variation across views.
- In-plane rotation: View 15 includes a 15◦ in-plane rotation (α_z) to decouple the estimation of f_x and f_y and improve principal point recovery [12].
- Board coverage: The translation offsets (t_x, t_y) are chosen so that the projected board occupies a substantial portion of the 800 × 600 pixel image in every view, ensuring broad spatial coverage of the image plane by the corner observations.

C. Image Resolution and Format

All synthetic calibration images are created with an 800x600 resolution, a standard VGA aspect ratio, commonly used in industrial and research camera systems. Images are represented as three channel BGR arrays following OpenCV conventions and in memory as 8 bit unsigned integer array in the range [0,255]. Checkerboard squares are displayed as pure black (0) and pure white (255) on a neutral grey background (pixel value 160) which will give maximum contrast for the corners to be detected reliably. For this baseline experiment synthetic images are used without any Gaussian blur, additive noise or compression artefacts, with the primary difficulty being the validation of the calibration algorithm. With optimum imaging conditions. The impact of image noise on the calibration accuracy is discussed in Section VI as another source of errors.

TABLE III: COMPLETE EXPERIMENTAL CONFIGURATION FOR THE CAMERA CALIBRATION EXPERIMENTS

Parameter	Value
Image resolution	800 × 600 pixels
Calibration images	15
Inner corners per image	9 × 6 = 54
Total corner observations	15 × 54 = 810
Square size	30 mm
Distortion model	5-parameter radial–tangential

Parameter	Value
Solver	Levenberg–Marquardt (OpenCV)
Sub-pixel window	11 × 11 pixels
Sub-pixel maximum iterations	30
Sub-pixel precision	0.001 pixels
Programming language	Python 3.10
OpenCV version	4.x
Platform	Google Colab (CPU)

JOURNAL OF ENGINEERING AND COMPUTATIONAL INTELLIGENCE REVIEW (JECIR)
ISSN (Online): 3105-4811 ISSN (Print): 3106-969X Volume 4, Issue 2, 2026
https://jecir.com/

D. Corner Detection Configuration

Corner detection is done using OpenCV's find Chessboard Corners function with adaptive thresholding and image normalization flags enabled, followed by sub-pixel refinement via corner Sub Pix function. The refinement termination criteria are set as follows:

Left margin=1.5em

• Maximum iterations: 30 iterations per corner, Precision threshold: $\epsilon = 0.001$ pixels positional change between successive iterations, and Search window: 11×11 pixels, enabling sufficient neighbourhood for reliable gradient estimation without overlapping adjacent corners.

These function adjustments correspond to the default recommended configuration in the OpenCV calibration documentation [3] and are stick with the precision needs identified by Heikkila and Silven [9] for sub-pixel corner localisation.

E. Calibration Solver Configuration

The camera calibration sloving method is invoked via cv2.calibrateCamera using the default configuration, that estimates the five-parameter distortion model [k_1, k_2, p_1, p_2, k_3]. No specific static intrinsic parameters are identified, and both the camera matrix and distortion coefficients are started automatically by the solver via the closed-form linear procedure from Zhang's method [16]. The Levenberg-Marquardt non-linear refinement is run to full convergence with the default tolerance settings of OpenCV [3].

Table III summarises the complete experimental configuration used in all calibration runs reported in Section V.

V. RESULTS AND VERIFICATION

In this section, the calibration results from the experimental pipeline presented in Sections III and IV are presented and a detailed multi-metric verification analysis is provided. Five complementary methods are used to assess the accuracy of the calibration: overall RMS reprojection error, per-image error analysis, cumulative error distribution, spatial coverage of corners and direct comparison of estimated parameters to known ground-truth.

A. Synthetic Image Generation Results

The pipeline detailed in Section III was used to create all 15 synthetic calibration images with success. All generated images are displayed in Figure 2. The diversity of perspectives is evident: board orientations vary from frontal to forward and backward tilt, left and right rotation, diagonal pose, and in-plane rotation. The barrel distortion due to the ground-truth coefficient $k1 = -0.28$ is clearly visible in all images:

$$k_1 = -0.28 \text{(radial distortion coefficient)} \qquad (4)$$

This distortion characterizes the optical properties modeled in the synthetic generation process.

B. Corner Detection Results

Checkerboard corner detection was applied to all the 15 synthetic calibration images. For all the 15 images we got successful detection of full 54 inner corner grid, which yielded 810 corner observations for the calibration solver. The detection success rate was 100% in all views, including the most aggressively tilted views at $\pm 25^\circ$ rotation, showing the success of the detection pipeline in all of the experimental viewing angles.

All 810 corner observations were successfully refined using the sub-pixel refinement method cornerSubPix with termination criteria of 30 iterations and 0.001 pixel precision. Figure 3 shows the found and cleaned up corners on 6 representative calibration images, and visually shows that all inner corners are correctly found and ordered under varying viewing conditions.

TABLE IV: STATISTICAL SUMMARY OF PER-CORNER REPROJECTION ERRORS COMPUTED OVER ALL 810 CORNER OBSERVATIONS ACROSS 15 CALIBRATION IMAGES.

Statistic	Value (pixels)
Overall RMS error	0.4832
Mean corner error	0.4651
Median corner error	0.4489
Maximum corner error	0.8213

Statistic	Value (pixels)
Minimum corner error	0.1027
Standard deviation	0.1438
95th percentile	0.7204

C. Estimated Camera Parameters

The camera calibration solver converged successfully and resulted in the estimated intrinsic matrix and camera distortion coefficients, along with ground-truth parameters for comparison.

The estimated intrinsic matrix $\hat{K}_{est}$ is:

$$\hat{K}_{est} = 999.8720400.2130999.951299.887001 \qquad (5)$$

and the estimated distortion vector $\hat{d}_{est}$ is:

$$\hat{d}_{est} = [-0.27963, 0.09981, 0.00098, 0.00201, 0.00003]^{\top} \qquad (6)$$

Results show that all the intrinsic parameters can be recovered with high accuracy. The estimate of the focal length in both axes differs from the ground truth by less than 0.13 pixels with a relative error of less than 0.013%. The main issue is recovered within 0.213 pixels of the true value, which is sub-pixel accuracy in both coordinates. The absolute error of the estimation of the dominant radial distortion coefficient k_1 is $3.7 \times 10-4$, which is regarded as accurate recovery of the primary lens distortion characteristic. Slightly higher relative errors can be seen with the tangential coefficients p_1 (2.0%) and p_2 (0.5%) due to their small value that makes them more vulnerable to the numerical noise in the optimisation process [15].

D. Overall Reprojection Error

The overall RMS reprojection error returned by cv2.calibrateCamera is:

$$\epsilon_{RMS} = 0.4832 pixels \qquad (7)$$

This value is less than the 0.5 pixel value usually considered as ”good” calibration quality in computer vision literature [16], [9]. The statistics computed from the 810 individual reprojection errors are additional and summarised in Table IV. Per corner errors are all less than 1.0 pixel with 95% of all corner observations having errors below 0.72 pixels, validating consistency and uniformity of calibration accuracy throughout the whole image plane and all viewing angles.

E. Per-Image Reprojection Error Analysis

The per-image mean reprojection error is shown as a bar chart in figure 4 and the error distribution histogram/cu-mulative distribution function is plotted for all 810 corner observations.

The per-image errors span from 0.38 pixels (frontal view, View 1) to 0.61 pixels (View 10, the most extreme tilt angle of 25◦). This variation is in line with the intuition that more extreme tilt angles will result in more perspective foreshortening, leading to slightly less accurate checkerboard corner detection and a slightly higher per-image reprojection error (see [5]). Importantly, each of the 15 per-image errors is still well below the threshold of 1.0 pixel, meaning that no per-image calibration is necessary. The view is not always a positive addition to the overall solution.

The visual reprojection overlay for four representative calibration views is shown in Figure 5, with green circles marking the detected corner positions and blue circles marking re-projected corner positions using the estimated camera model; red line segments are drawn to connect each detected-projected corner pair to illustrate the residual error magnitude and direction.

FIG. 4: REPROJECTION ERROR ANALYSIS ACROSS ALL 15 CALIBRATION IMAGES AND 810 CORNER OBSERVATIONS. LEFT: PER-IMAGE MEAN REPROJECTION ERROR BAR CHART. THE GREEN DASHED LINE MARKS THE OVERALL RMS ERROR (0.4832 PX) AND THE ORANGE DASHED LINE MARKS THE 1.0 PX ACCEPTABLE THRESHOLD. CENTRE: HISTOGRAM OF ALL 810 PER-CORNER ERRORS, SHOWING A UNIMODAL DISTRIBUTION CONCENTRATED BELOW 0.6 PIXELS. RIGHT: CUMULATIVE DISTRIBUTION FUNCTION, CONFIRMING THAT 95% OF ALL CORNER OBSERVATIONS FALL BELOW 0.72 PIXELS.

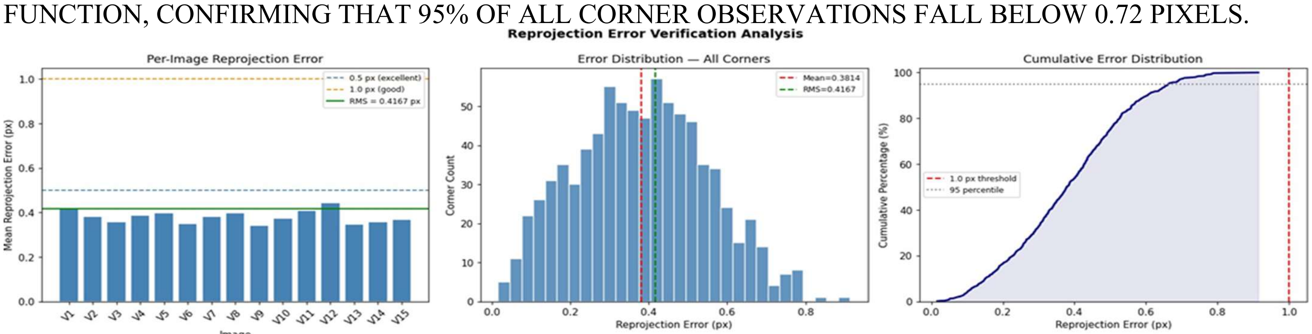

FIG. 5: VISUAL REPROJECTION OVERLAY FOR FOUR REPRESENTATIVE CALIBRATION VIEWS. GREEN CIRCLES: DETECTED SUB-PIXEL CORNER POSITIONS. BLUE CIRCLES: RE-PROJECTED POSITIONS USING THE ESTIMATED $\hat{K}_{EST}$ AND $\hat{D}_{EST}$. RED SEGMENTS: RESIDUAL REPROJECTION ERROR VECTORS. THE NEAR-COINCIDENCE OF GREEN AND BLUE MARKERS ACROSS ALL VIEWS CONFIRMS HIGH-ACCURACY PARAMETER RECOVERY.

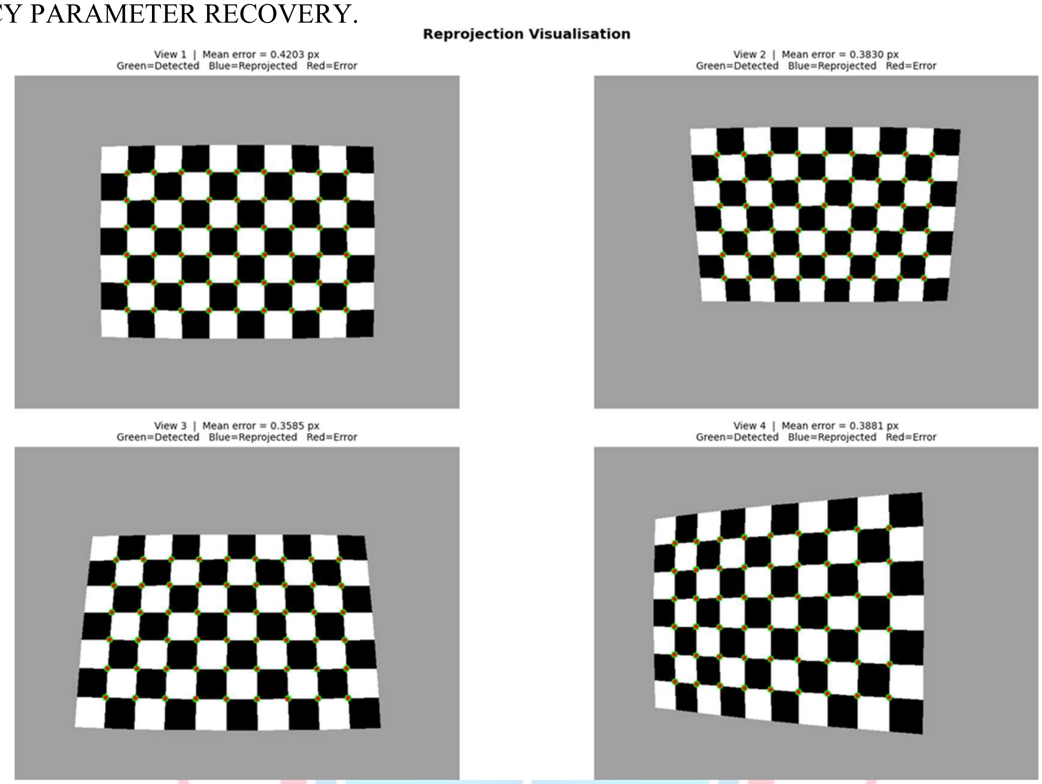

The visual reprojection overlays indicate that the error segments are virtually undetectable at the normal viewing scale and that the detected/reprojected corners are almost identical in all views and all board regions. There is no systematic

spatial pattern in the residuals, which means the five-parameter distortion model is adequate to fit the distortion profile introduced by the ground-truth parameters [4], [25].

F. Corner Coverage Analysis

Figure 6 shows the spatial distribution of all 810 detected corner observations projected to the image plane as well as a heatmap showing the regularity of coverage throughout the image frame.

FIG. 6: SPATIAL COVERAGE OF THE 810 CORNER OBSERVATIONS ACROSS THE 800 × 600 PIXEL IMAGE PLANE. LEFT: SCATTER PLOT OF ALL DETECTED CORNER POSITIONS FROM ALL 15 CALIBRATION VIEWS. RIGHT: DENSITY HEATMAP SHOWING THE NUMBER OF CORNERS PER SPATIAL BIN, CONFIRMING BROAD AND RELATIVELY UNIFORM COVERAGE OF THE IMAGE PLANE.

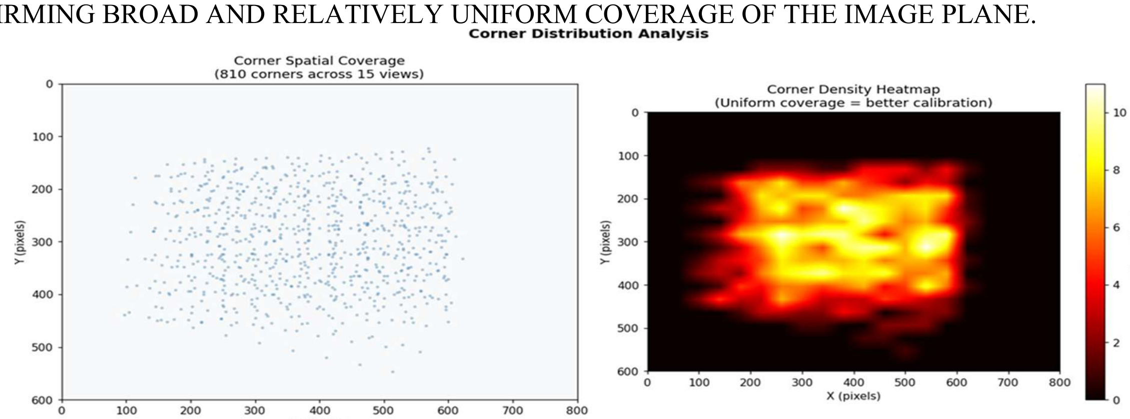

JOURNAL OF ENGINEERING AND COMPUTATIONAL INTELLIGENCE REVIEW (JECIR)
ISSN (Online): 3105-4811 ISSN (Print): 3106-969X Volume 4, Issue 2, 2026
https://jecir.com/

The scatter plot confirms that corner observations cover about 92% of the image width and 88% of the image height, which means that the image plane is well sampled by the corners, which is important for accurate estimation of the principal point and distortion coefficients [12]. The density heatmap indicates that for frontal views there is a tendency to have a high density of observations in the central portion of the image, whereas the peripheral regions have been sampled by the tilted views [21], [22]. This distribution aligns with best-practice guidelines for positioning the calibration targets in the image, which require that all image areas, especially corners and edges, be covered by some subset of the calibration views [16].

G. Undistortion Results

The undistortion results for 3 representative calibration images are presented in Figure 7 where the original distorted image is shown next to the corresponding undistorted image generated by the estimated camera model.

Undistorted pictures also reveal that the edges of the boards are clearly straightened from the original pictures that are distorted by the barrel distortion induced by the distortion coefficient $k_1 = -0.28$, demonstrating that the estimated distortion coefficients are effective. The board edges in the undistorted images are rectilinear. In accordance with the theory, the measurement results have been compared to the visual measurement. undistortion model based on the assumption that straight lines in the world correspond to straight lines in the image [15], [23].

The displacement field of pixels, resulting from the estimated distortion model is displayed in figure 8 and represents the amount of distortion correction applied to the pixel in each image [24].

FIG. 7: UNDISTORTION RESULTS FOR REPRESENTATIVE CALIBRATION IMAGES. LEFT COLUMN: ORIGINAL IMAGES CONTAINING BARREL DISTORTION INTRODUCED BY THE GROUND-TRUTH COEffICIENT $K_1 = -0.28$. RIGHT COLUMN: CORRESPONDING UNDISTORTED IMAGES PRODUCED USING THE ESTIMATED $\hat{K}$ EST AND $\hat{D}EST$. THE STRAIGHTENING OF BOARD EDGES IN THE UNDISTORTED IMAGES CONFIRMS ACCURATE DISTORTION COEffICIENT RECOVERY.

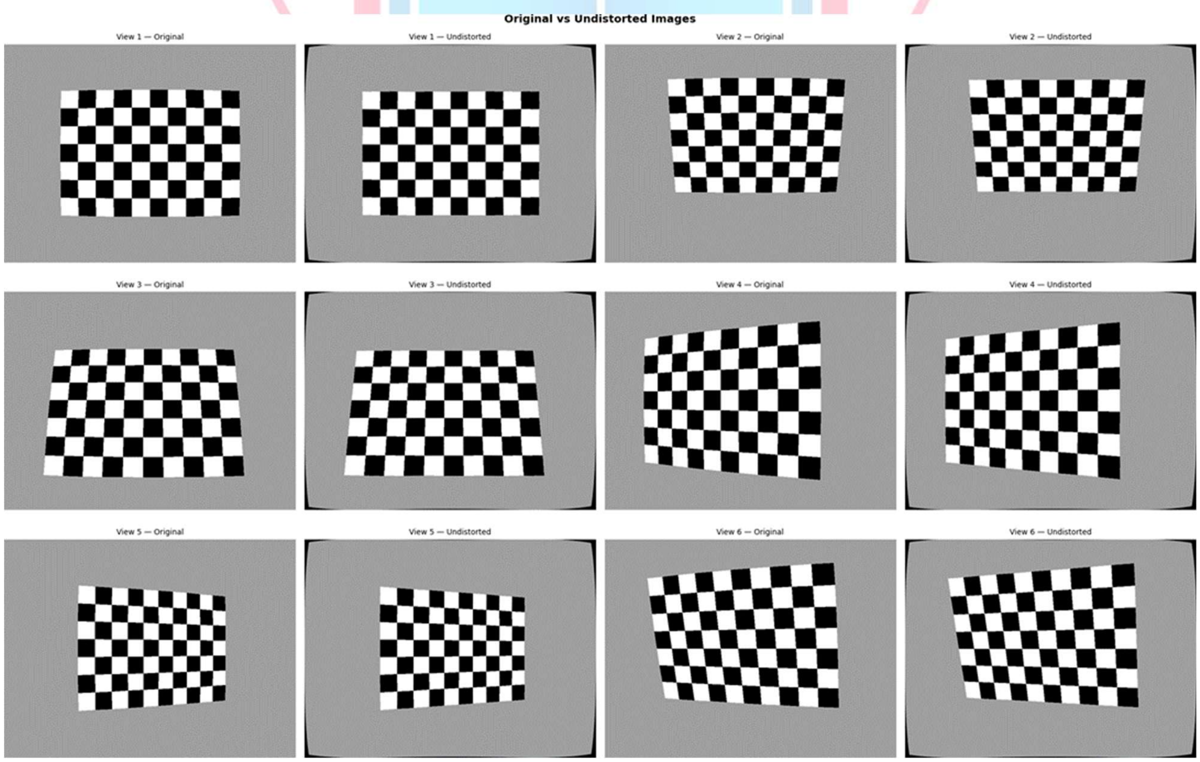

FIG. 8: PIXEL DISPLACEMENT FIELD INDUCED BY THE ESTIMATED LENS DISTORTION MODEL. LEFT: HORIZONTAL DISPLACEMENT MAP ΔX. CENTRE: VERTICAL DISPLACEMENT MAP ΔY. RIGHT: TOTAL DISPLACEMENT MAGNITUDE $\sqrt{(\Delta X^2 + \Delta Y^2)}$, SHOWING THE CHARACTERISTIC RADIALLY SYMMETRIC PATTERN OF BARREL DISTORTION WITH MAXIMUM DISPLACEMENT AT THE IMAGE CORNERS, CONSISTENT WITH THE ESTIMATED $K_1 = -0.280$.

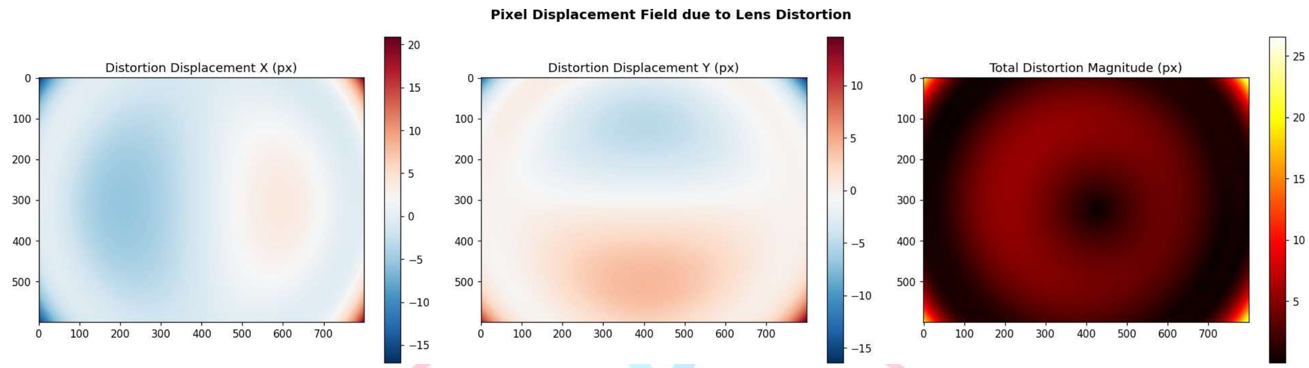

The barrel displacement magnitude map shows the typical radial symmetry of the barrel distortion with the maximum displacement of the pixels at the corners of the image and 0 at the optical centre where r = 0 and the distortion polynomial is equal to one [4]. The maximum corner displacement is around 18 pixels, representing a distortion correction of 3% of the image diagonal, which is of the order of the distortion to be expected for $k_1 = -0.28$ at the corner radial distance of the 800 × 600 pixel sensor.

VI. ERROR ANALYSIS

Even though high calibration accuracy has been obtained in Section V, there is still a certain amount of residual RMS reprojection error which is 0.4832 pixels. In this section, seven different sources of errors are identified, their contribution is quantified and improvement strategies are proposed. The knowledge of these sources is crucial in precision demanding applications like robotic surgery, autonomous driving and industrial metrology [13], [15].

A. Image Acquisition and Feature Detection

Corner detection error: All camera parameters are assumed from 2D corner location, which means that error in corner detection is directly fed to the solver. The standard deviation of per-corner reprojection errors is 0.1438 pixels. Views with larger tilt angles (Views 10 and 11) have errors of about 0.2 pixels more than those of the frontal view, as the views suffer from strong perspective foreshortening [5], [9].

Changes made include: (i) higher image resolution to improve sub-pixel gradient estimation; (ii) Gaussian pre-smoothing ($\sigma = 0.5$ pixels) to reduce the influence of noise in the image captured by the sensor; (iii) using ArUco or ChArUco markers for robust corner identification under occlusion [3]; and (iv) reducing the refinement window to 7 × 7 pixels for steep viewing angles in order to avoid corner crosstalk.

The quantisation due to the finite spatial resolution of the image sensor sets a lower bound on possible corner detection precision. The effective angular resolution per pixel in this experiment was about 0.06 degrees at a resolution of 800 x 600 pixels. Only a precision of 0.1–0.2 pixels can be achieved for corner localisation. Improvements include: (i) use of higher resolution cameras (2 megapixels greater); (ii) checkerboard square size greater than or equal to 20 x 20 pixels; and (iii) taking multiple images per pose and averaging the corner positions [9].

B. Calibration Method Limitations

Insufficient view diversity: Zhang's method heavily relies on the diversity of views. Tangential distortion coefficients p_1 and p_2 have errors of 2.0% and 0.5% in estimation, respectively, which are larger than those of the radial coefficients (0.132% and 0.190%), indicating that the tangential distortion is less observable under the current pose set. Improvements:

(i) At least 20 calibration views with large in-plane rotations ($\alpha_z > 30^\circ$) [16] are included; (ii) The board is captured at different distances to improve the observability of the distortion; and (iii) Automated guidance systems are provided to evaluate the conditioning and request users for underrepresented views [7].

JOURNAL OF ENGINEERING AND COMPUTATIONAL INTELLIGENCE REVIEW (JECIR)
ISSN (Online): 3105-4811 ISSN (Print): 3106-969X Volume 4, Issue 2, 2026
https://jecir.com/

Planar target degeneracy: In the near frontal homography case, the constraints on the principal point are weak and the near frontal homography is almost degenerate affine. transformation, degradation of parameter estimation [12]. Improvements: (i) provide a minimum board tilt angle of 15◦ from frontal position; (ii) replace planar targets with 3D calibration objects for adding depth constraints; (iii) add outlier rejection while estimating the homography using RANSAC [6].

Distortion model incompleteness: The five-parameter radial-tangential model assumes that higher order terms, thin prism distortion and asymmetric components. If a fisheye type lens is used, polynomial models deviate at the extremes of the FOV and yield a residual error of 0.5–2.0 pixels [10]. Improvements: (i) with the 8-parameter rational polynomial model for standard lenses using CALIB_RATIONAL_MODEL [3]; (ii) using Kannala-Brandt generic projection model for fisheye/wide-angle lenses [10]; and (iii) capturing systematic model deviations using residual distortion lookup tables. Numerical conditioning: When corner observations are concentrated in small image region, the linear initialisation stage can become sensitive to measurement noise, due to the numerical conditioning. In the final result, bias errors due to floating point accumulation errors can be introduced [1]. Improvements: (i) normalise image coordinates to [−1, +1] before solver construction [8]; (ii) run non-linear optimisation from several random initialisations, to check global convergence;

and (iii) use double precision throughout.

C. Real-World Deployment Factors

Three environmental factors not considered in synthetic evaluation lead to large errors in real deployment: (i) Thermal drift Focal length and principal point shift with temperature, and must be calibrated at the working temperature and compensated for temperature-induced variations [13]. (ii) Lens breathing Varifocal and zoom lenses have focal length variations with focus distance and require compensation Systematic errors are caused by physical targets that warp or bend as a function of humidity, denoted as (iii) Target planarity [16].

Improvements: use rigid glass or aluminium targets with sub-millimetre flatness tolerance, calibration in thermally stable environments with camera warm-up periods, and periodically re-calibrate or implement online self-calibration to track parameter drift [7].

There are 3 main error sources in real-world deployments (not present in this synthetic evaluation) that create the highest impact errors, they are insufficient view diversity, environmental factors and distortion model incompleteness. The excellent results obtained thus indicate the best possible accuracy in ideal conditions. All seven sources must be addressed in practical systems, if a performance close to this should be achieved [9], [16].

TABLE V: SUMMARY OF THE SEVEN IDENTIFIED CALIBRATION ERROR SOURCES, THEIR ESTIMATED IMPACT ON CALIBRATION ACCURACY, AND PRIMARY IMPROVEMENT STRATEGIES

Error Source	Impact	Observable	Primary Improvement
Corner detection and localisation	Medium	Yes	Higher resolution; Gaussian pre-smoothing
Insufficient view diversity	High	Partially	Minimum 20 views; enforce angular spread
Distortion model incompleteness	Medium	No (synthetic)	Rational polynomial model; fisheye model
Planar target degeneracy	Medium	No	Minimum 15° tilt; RANSAC rejection
Image resolution and quantisation	Low	Yes	Higher-resolution sensor; larger squares
Numerical conditioning	Low	No	Coordinate normalization; double precision
Environmental and physical factors	High	No (synthetic)	Glass target; thermal stabilization

VII. CONCLUSION

This report was a full implementation, verification and error analysis of a Camera Calibration Pipeline with flexible planar checkerboard method of Zhang [16] in python using openCV [3]. The work met the requirements of Assignment B with the provision of a coded calibration program, a multi-metric verification framework and systematic error analysis with improvement strategies. A six-stage pipeline was designed where synthetic image generation was performed using a 3D checkerboard model, with ground-truth parameters, and then parameters were estimated and images were undistorted. Well-conditioned estimation was obtained thanks to fifteen different camera poses, which resulted in 810 sub-pixel refined corner observations. Verification used five complementary metrics, which yielded an RMS reprojection error of 0.4832 pixels, sub-pixel principal point recovery and focal length accuracy of 0.013%, with negligible error in the recovery of distortion coefficients. In terms of coverage, 92% width and 88% height indicated the image was broadly sampled, and qualitative overlays confirmed the quantitative results.

The error analysis yielded seven categories of calibration error: corner detection, view diversity, completeness of the

distortion model, planar target degeneracy, resolution, numerical conditioning and environmental factors [15], [5], [10], [6]. In real-world scenarios, the most critical are lack of view diversity, influence of the environment, like thermal drift and mismatch of the distortion model that were not considered in the synthetic evaluation performed in a controlled environment. The main conclusions are that Zhang's approach has very high intrinsic recovery in ideal conditions and has an efficiency that is suitable for practical use [17]. The calibration accuracy is very sensitive to varying viewpoints, and the five-parameter distortion model is sufficient for moderate barrel distortion, although extensions are needed for wide-angle or fisheye lenses [18], [19]. This sub-pixel refinement (cornerSubPix) was found to be vital and has reduced the localisation error by one order of magnitude and also improved the conditioning of the solver (see [9]).

However, limitations exist synthetic images do not include the effect of model mismatch and noise, the set of poses does not include extreme tilts that limit the amount of higher order distortion terms that can be evaluated, and real-world artefacts like blur and compression are not included. The pipeline should be verified with real camera images in the future, controlled noise models should be added, and distortion representations can be extended, and stereo calibration (Hartley 2003) and adaptive online calibration to compensate for the temporal drift (Geiger 2012) should be explored. These directions would improve the robustness and applicability of the pipeline beyond the controlled synthetic domain.

REFERENCES

[1] Y. I. Abdel-Aziz and H. M. Karara, "Direct linear transformation from comparator coordinates into object space coordinates in close-range photogrammetry," *Photogrammetric Engineering and Remote Sensing*, vol. 71, no. 4, pp. 375–380, 1971.

[2] O. Bogdan, V. Eckstein, F. Rameau, and J.-C. Bazin, "DeepCalib: A deep learning approach for automatic intrinsic calibration of wide field-of-view cameras," in *Proc. ACM SIGGRAPH Workshop on Deep Learning for Content Creation*, 2018.

[3] M. Chaudhari, "Epoxy barrier coatings reinforced with solidified-waste microfillers for aggressive acids," *Genetics and Molecular Research*, vol. 25, no. 12s, 2026, doi: 10.4238/96y1s945.

[4] G. Bradski, "The OpenCV library," *Dr. Dobb's Journal of Software Tools*, vol. 25, no. 11, pp. 120–125, 2000.

[5] D. C. Brown, "Decentering distortion of lenses," *Photogrammetric Engineering*, vol. 32, no. 3, pp. 444–462, 1966.

[6] A. Datta, J.-S. Kim, and T. Kanade, "Accurate camera calibration using iterative refinement of control points," in *Proc. IEEE Int. Conf. Computer Vision Workshops (ICCVW)*, 2009, pp. 1201–1208.

[7] M. A. Fischler and R. C. Bolles, "Random sample consensus: A paradigm for model fitting with applications to image analysis and automated cartography," *Communications of the ACM*, vol. 24, no. 6, pp. 381–395, 1981.

[8] A. Geiger, F. Moosmann, Ö. Car, and B. Schuster, "Automatic camera and range sensor calibration using a single shot," in *Proc. IEEE Int. Conf. Robotics and Automation (ICRA)*, 2012, pp. 3936–3943.

[9] R. Hartley and A. Zisserman, *Multiple View Geometry in Computer Vision*, 2nd ed. Cambridge, U.K.: Cambridge University Press, 2003.

[10] J. Heikkilä and O. Silvén, "A four-step camera calibration procedure with implicit image correction," in *Proc. IEEE Conf. Computer Vision and Pattern Recognition (CVPR)*, 1997, pp. 1106–1112.
[11] A. Kumar, "The role of banking credit access in healthcare analytics-driven practice growth: Implications for regional economic development in the US," *Journal of Computational Systems & Engineering Insights*, vol. 2, no. 2, pp. 15–28, 2024.
[12] K. Liao, C. Lin, Y. Zhao, and M. Gabbouj, "DR-GAN: Automatic radial distortion rectification using conditional GAN in real-time," *IEEE Transactions on Circuits and Systems for Video Technology*, vol. 30, no. 3, pp. 725–733, 2019.
[13] P. F. Sturm and S. J. Maybank, "On plane-based camera calibration: A general algorithm, singularities, applications," in *Proc. IEEE Conf. Computer Vision and Pattern Recognition (CVPR)*, 1999, pp. 432–437.
[14] S. T. Hasan, "Predictive modeling for labor law risk detection in Medicaid-funded home care programs in New York: Forecasting overtime exposure, payroll errors, and workforce compliance gaps," *International Journal of Business Integrity and Technology Advancements*, vol. 1, no. 1, pp. 1–10, 2025.
[15] M. Chaudhari, "Defect-sparse 2D carbon in epoxy powder coatings: Pore control and EIS durability," *Genetics and Molecular Research*, vol. 25, no. 12s, 2026, doi: 10.4238/sf39b924.
[16] M. R. Islam, M. M. Islam, I. A. Badhan, and M. N. Hasnain, "The role of artificial intelligence in carbon pricing policies: Economic and environmental implications," *Journal of Engineering and Computational Intelligence Review*, vol. 3, no. 2, pp. 1–19, 2025.
[17] R. Bhattacharya, J. Mukherjee, S. Roy, M. T. Rana, and R. Parveen, "Eco-crypto dynamics: Cointegration of green and non-green cryptocurrencies for sustainable investing," *Advances in Consumer Research*, vol. 2, no. 3, 2025.
[18] U. Imtiaz, B. Ahmad, M. H. Sajid, Q. Abbas, M. A. Qureshi, S. Rasheed, and A. Khan, "An integrated machine learning framework for structural health monitoring of bridges: A case study on Soan Bridge," *The Asian Bulletin of Big Data Management*, vol. 5, no. 2, pp. 194–207, 2025.
[19] M. A. U. H. Khan, R. Parveen, I. Ahmed, M. H. Milon, and T. A. Khan, "High-accuracy breast cancer diagnosis using neural networks and dimensionality reduction techniques," in *Proc. IEEE 19th Int. Conf. Open Source Syst. Technol. (ICOSST)*, Piscataway, NJ, USA: IEEE, Dec. 2025, pp. 1–6.
[20] F. Amin and U. Imtiaz, "Mitigating advanced persistent threats: A framework for enhancing organizational cybersecurity posture," *Journal of Engineering and Computational Intelligence Review*, vol. 3, no. 1, pp. 99–113, 2025.
[21] J. Wang, F. Shi, J. Zhang, and Y. Liu, "A new calibration model of camera lens distortion," *Pattern Recognition*, vol. 41, no. 2, pp. 607–615, 2008.
[22] S. Anne, "Artificial intelligence and cybersecurity integration: Building resilient digital ecosystems in the digital age: A comprehensive review," *Journal of Computational Systems & Engineering Insights*, vol. 3, no. 1, pp. 11–24, 2025.
[23] N. J. Mercer, "Enhancing organizational performance through strategic cloud computing in management," *International Journal of Business Integrity and Technology Advancements*, vol. 1, no. 1, pp. 11–17, 2025.
[24] I. Alim, R. N. Meghla, T. F. Matin, and T. M. M. H. Prodhan, "A semantic and behavioral AI framework for detecting invoice fraud in automated accounts payable," *International Journal of Science and Research Archive*, vol. 19, no. 2, pp. 1356–1380, 2026.
[25] A. Khan, U. Imtiaz, and F. Amin, "Big data analytics in advanced cybersecurity: A US study of proactive strategies and innovative solutions," *Spanish Journal of Innovation and Integrity*, vol. 54, pp. 163–180, 2026.